Article

Satellite Evidence for Increasing in Terrestrial Evapotranspiration over the Contiguous United States from 2001 to 2022

Lu Liu [1], Yunjun Yao [1,*], Yufu Li [2], Zijing Xie [1], Jing Ning [1], Ruiyang Yu [1], Jiahui Fan [1], Yixi Kan [3], Luna Zhang [1] and Jia Xu [4]

1. State Key Laboratory of Remote Sensing Science, Faculty of Geographical Science, Beijing Normal University, Beijing 100875, China; liululu@mail.bnu.edu.cn (L.L.); xiezijing@mail.bnu.edu.cn (Z.X.); njing@mail.bnu.edu.cn (J.N.); yuruiyang@mail.bnu.edu.cn (R.Y.); 202221051094@mail.bnu.edu.cn (J.F.); 202321051212@mail.bnu.edu.cn (L.Z.)
2. Jincheng Meteorological Administration, Jincheng 048026, China; qxtlyf@163.com
3. School of Geography and Planning, Chengdu University of Technology, Chengdu 610059, China; 2022020025@stu.cdut.edu.cn
4. Department of Infrastructure Engineering, Faculty of Engineering & IT, University of Melbourne, Melbourne, VIC 3010, Australia; jiax5@student.unimelb.edu.au
* Correspondence: yaoyunjun@bnu.edu.cn

Abstract: Evapotranspiration (ET) is a key process in the eco-hydrological cycle of a basin and a reliable indicator of climate change. However, the spatiotemporal alterations of ET in the contiguous United States (CONUS) over the recent two decades remain largely uncertain. In this study, we used the recently proposed Priestley–Taylor (PT)-SinRH model to estimate the ET of CONUS during 2001–2022 based on satellite and reanalysis data. The results showed that the PT-SinRH model yielded superior performance at eddy covariance (EC) sites, and the root-mean-square error (RMSE) ranged from 6.0 to 33.5 W/m^2, the Kling–Gupta efficiency (KGE) ranged from 0.22 to 0.66. The annual mean value of ET in CONUS from 2001 to 2022, estimated by the PT-SinRH model, was 42.54 W/m^2, and the spatial pattern of seasonal and annual ET variations increased from west to east. From 2001 to 2022, seasonal and annual ET of CONUS showed linear trends, with an average increase of 0.76 $W/m^2/da$ ($p < 0.05$). The ET in the east of CONUS exhibited a rate of increase at 1.45 $W/m^2/da$, and the ET in the west of CONUS exhibited a rate of increase at 0.42 $W/m^2/da$ ($p < 0.05$). Importantly, our analysis of ET trends highlights that the change of precipitation (*P*) and normalized difference vegetation index (*NDVI*) exerts a significant impact on the change of ET over CONUS.

Keywords: PT-SinRH model; evapotranspiration; contiguous United States; spatial-temporal variations; controlling factors

1. Introduction

Terrestrial evapotranspiration (ET) plays a significant role in the water balance of terrestrial ecosystems as it encompasses the total loss of water from plant transpiration and evaporation from land surfaces (soil, snow, and vegetation) [1–3]. An accurate understanding of ET is essential for comprehending the water and energy balance in a region. As a key surface state variable, high-precision and long-time series ET products play an important role in many related fields, such as drought monitoring [4], forest ecosystem health and productivity evaluation, water use efficiency evaluation, global climate change [5], and other research areas [6]. Especially the accurate simulation of forest ET plays a significant role in forest water resource management and effective utilization, sustainable development of forestry, and even global climate change response. Meanwhile, as a major agricultural producer and important forest resource location, the contiguous United States (CONUS) faces challenges in water resource management and pressure from climate

change. Accurate ET also holds great importance for formulating effective water resource management and forest conservation policies. However, much uncertainty remains concerning the changes in ET over recent decades and the potential factors contributing to these changes [7]. Many researchers are also aware of the importance of long-term trend identification of ET, which can timely and accurately understand the hydrological and climatic trends at the regional scale [8].

At present, the existing methods for estimating ET mainly include statistical or empirical models [9–11], remotely sensed methods [12–14] and land surface models [15–18]. Based on these methods, various regional ET products have been generated in the last few decades [19], such as Gridded FLUXNET ET, GFET [9], moderate resolution imaging spectroradiometer (MODIS) ET, MOD16 [20,21], operational simplified surface energy balance (SSEBop) model [22], global land surface satellite (GLASS) ET [23] and global land evaporation and Amsterdam model ET, GLEAM [24,25]. However, there are significant differences in the performance of these products in simulating the ET because of the differences in model structures and dominant variables [26,27]. For example, Velpuri et al. validated MOD16 and SSEBop ET products (1 km) based on MODIS using GFET and basin water balance ET in the CONUS. The results show that the relative error range between the ET estimated value and the ground observation value is 14%–44%, and the relative performance of the two models is different in space [28]. Therefore, there is still great uncertainty in the temporal and spatial variation of ET over long-time series in the CONUS, and the uncertainty of various ET products produced by different methods ranges from 4–15 mm/month [27], which may be affected by model parameterization, spatial variation, heterogeneity, and other factors. Most previous studies have shown that the main factor determining changes in ET trends is the limitation of surface water supply [29,30]. However, some studies suggest that changes in ET trends may also be influenced by temperature and vegetation conditions [31–33].

As the most widely used algorithm, the Priestley–Taylor algorithm in the Jet Propulsion Laboratory (PT-JPL) [34] integrated remote sensing information so that the ET of diverse ecosystems and biomes can be estimated at regional scales [35], and previous studies have demonstrated that the PT-JPL outperforms other ET models [36]. Recently, Xie et al. [37] proposed a new PT-SinRH model based on the PT-JPL, which has been used to estimate ET in the CONUS. As an improved version of the PT-JPL, PT-SinRH replaces the RH^{VPD} (vapor pressure deficit, VPD) with a sine expression of relative humidity (RH) to represent the soil moisture (SM) restriction. This substitution enchance the accuracy of ET estimation by eliminating the influence of VPD uncertainty on ET. According to validations conducted at eddy covariance (EC) sites with various land cover types throughout the CONUS, the Kling–Gupta efficiency (KGE) between measured and predicted ET increased by 8% for the PT-SinRH compared to the PT-JPL, while the root-mean-square error (RMSE) decreased by about 3.5 W/m^2 on a daily scale. However, there is a scarcity of comparable research using the PT-SinRH model and reanalysis data to simulate ET over CONUS. There is an urgent need to investigate the spatiotemporal variations of the long-term reaction of ET to climatic change in the CONUS.

In this study, we applied the PT-SinRH model to quantify ET in CONUS and generated the daily ET products with a spatial resolution of 0.05° based on satellite and meteorological reanalysis data from 2001 to 2022, providing an effective reference for addressing the lack of high spatiotemporal ET products in CONUS. We have three main objectives. Firstly, we evaluate the effectiveness of the PT-SinRH with data from 28 EC sites in CONUS. Secondly, we analyze the spatiotemporal patterns of annual and seasonal ET from 2001 to 2022 in the CONUS. Finally, we detect the controlling factors of annual and seasonal variability and trends change of ET in the CONUS from 2001 to 2022.

2. Study Area and Data

2.1. Study Area

The CONUS comprises a diverse spectrum of ecosystems and climates, making it an ideal study area for evaluating the PT-SinRH model. The CONUS, which was divided into east and west by the Mississippi River and situated between longitudes 70°–130° E and latitudes 25°–49° N (Figure 1), includes various climatic zones due to its varying topography. The climate across the CONUS varies from arid deserts in the southwest to humid subtropical conditions in the southeast and from polar climate in Alaska to temperate forests in the Pacific Northwest.
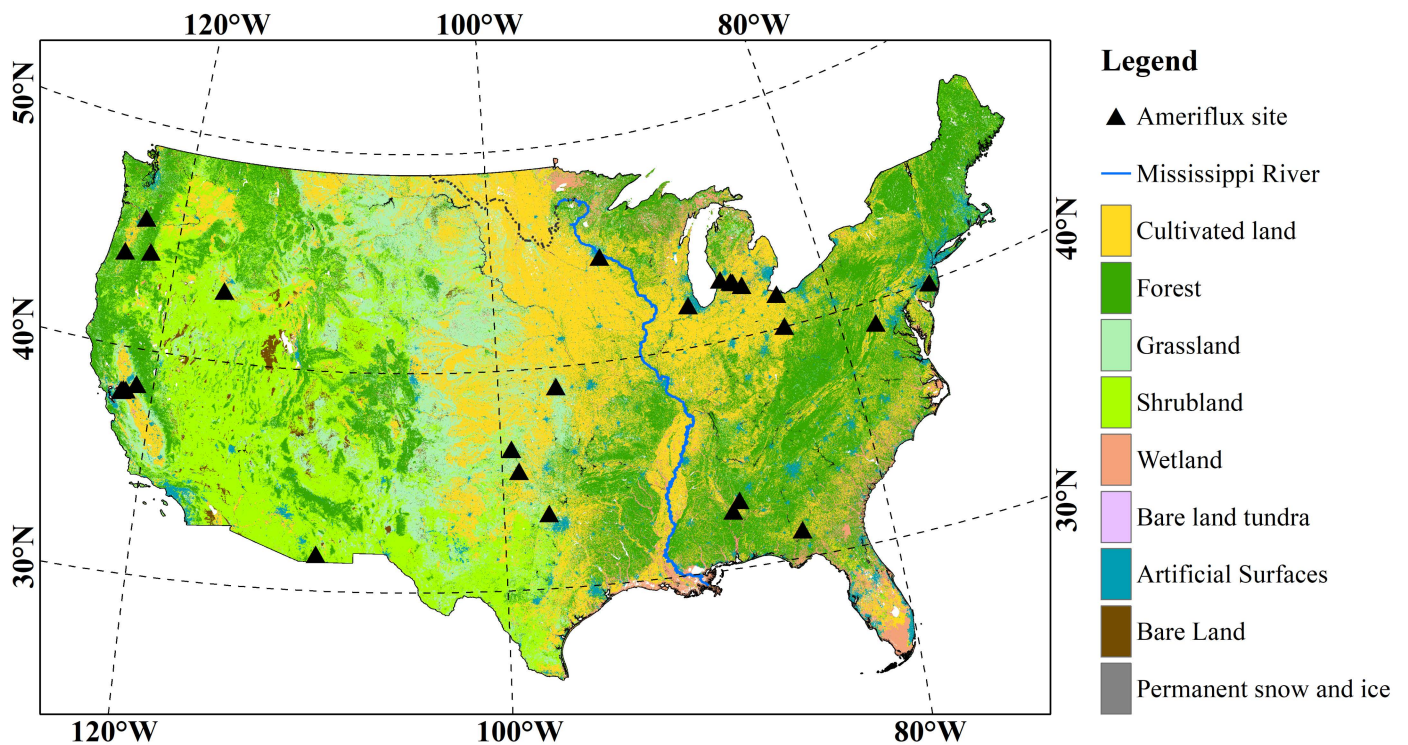

Figure 1. Study area.

The CONUS features a diverse range of land cover types (Figure 1), and the global land cover dataset (GlobeLand30) (30 m) was used as the background of the study area (http://www.globeland30.org, accessed on 16 February 2024). These ecosystems are situated across diverse geographical and climatic regions. In this study, the CONUS is divided into east and west based on the Mississippi river, and each contributing differently to the climate and evapotranspiration. Furthermore, the CONUS hosts the extensive Ameriflux network (https://ameriflux.lbl.gov, accessed on 10 April 2024) that provides superior -quality measurements of critical elements essential for estimating evapotranspiration. We evenly chose 28 EC sites, and the sites' locations are marked with triangles in Figure 1.

2.2. Data

2.2.1. Ground Measurements

This study utilized ET observations from ground-based eddy covariance (EC) sites to evaluate the effectiveness of the PT-SinRH model. Observations were sourced from 28 AmeriFlux sites (https://ameriflux.lbl.gov, accessed on 10 April 2024), distributed across diverse terrains within the CONUS, covering a range of climatic conditions. These datasets were integrated with hourly or half-hourly meteorological measurements, including average temperature (T_a), maximum air temperature (T_{max}), RH, net radiation (R_n), ground heat flux (G), and ET. According to the method proposed in Reichstein et al. [38], daily

ET observations were harmonized with half-hourly data to maintain a uniform temporal resolution for ET. Data was deemed missing if more than 25% of the daily observations were absent. The Bowen ratio closure approach was employed to correct the energy imbalance in the EC measurements [39], as suggested by Foken [40].

2.2.2. Satellite and Reanalysis Data

We utilized the normalized difference vegetation index (NDVI) of the GLASS products from 2001 to 2022, which were generated using advanced very high-resolution radiometer (AVHRR) data, referred to as GLASS-AVHRR (https://glass-product.bnu.edu.cn/, accessed on 14 April 2024). The spatial resolution of GLASS-AVHRR NDVI is 0.05°, and the temporal resolution is eight days [41].

Additionally, we incorporated meteorological variables T_a, T_{max}, RH, G, R_n, and precipitation (*P*) from the Modern-Era Retrospective Analysis for Research and Applications, version 2 (MERRA-2) from 2001 to 2022 (https://disc.gsfc.nasa.gov/datasets, accessed on 31 May 2024). MERRA-2 is produced by NASA's Global Modeling and Assimilation Office (GMAO) using atmospheric reanalysis data, which integrates extensive satellite observations, including novel data types such as aerosols, microwaves, and hyperspectral radiation. For improved data utilization, hourly MERRA-2 data with a spatial resolution of $1/2° \times 2/3°$ were aggregated into daily values. At the same time, the bilinear interpolation method is used to increase the spatial resolution to 0.05° to align with the spatial resolution of GLASS-AVHRR NDVI. Then, we can generate ET products at a 0.05°.

3. Methods

3.1. PT-SinRH Model

In the PT-JPL, RH^{VPD} is employed to characterize soil moisture constraint, but *VPD* has great uncertainty. To reduce the influence of *VPD* on ET, Xie et al. [37] proposed the PT-SinRH model, which characterizes the soil moisture constraint by introducing a sinusoidal function of RH. It can be represented as follows:

ET was calculated as the sum of the soil evaporation (ET_s), canopy transpiration (ET_c), and interception evaporation (ET_i):

$$ET = ET_s + ET_c + ET_i, \tag{1}$$

To obtain a more accurate estimation of soil evaporation (ET_s), the PT-SinRH model introduces *RH* and sine function to characterize *SM* constraint (f_{sm}). *ETs* can be described as follows:

$$ET_s = (f_{wet} + f_{sm}(1 - f_{wet}))\alpha \frac{\Delta}{\Delta + \gamma}(R_{ns} - G), \tag{2}$$

$$f_{wet} = RH^4, \tag{3}$$

$$f_{sm} = RH - \sin(2\pi RH)/(2\pi), \tag{4}$$

$$R_{ns} = R_n exp(-k_{Rn} LAI), \tag{5}$$

$$LAI = -\ln(1 - f_c)/k_{PAR}, \tag{6}$$

where f_{wet} is the relative land wetness based on Equation (3) of Fisher et al. [34], α is Priestly Taylor coefficient (1.26) [42], and γ is the psychrometric constant (0.066 kPa/°C). The Δ is the slope of the saturated vapor pressure curve. *G* is the ground heat flux. R_{ns} is net radiation to the soil, and R_n is net radiation. $k_{Rn} = 0.6$, *LAI* is total (green + non-green) leaf area index, $f_c = f_{IPAR}$ and $k_{PAR} = 0.5$.

The canopy transpiration (ET_c) can be described as follows:

$$ET_c = (1 - f_{wet})f_g f_M f_T \alpha \frac{\Delta}{\Delta + \gamma} R_{nc}, \tag{7}$$

$$f_g = \frac{f_{APAR}}{f_{IPAR}}, \tag{8}$$

$$f_M = \frac{f_{APAR}}{f_{APARmax}}, \tag{9}$$

$$f_T = exp\left[-\left(\frac{T_{max} - T_{opt}}{\lambda}\right)^2\right], \tag{10}$$

$$R_{nc} = R_n - R_{ns}, \tag{11}$$

$$f_{APAR} = m_1 SAVI + b_1, \tag{12}$$

$$f_{IPAR} = m_2 NDVI + b_2, \tag{13}$$

where f_g is the green canopy fraction, f_M is the plant moisture constraint, and f_{APAR} and f_{IPAR} are the fraction of *PAR* absorbed by green vegetation cover and a fraction of *PAR* intercepted by total vegetation, respectively, which are calculated based on Equations (12) and (13), respectively. The $m_1 = 1.2 \times 1.136$, $b_1 = 1.2 \times (-0.04)$, and $m_2 = 1.0$, $b_2 = -0.05$ (assumes $0.05 < NDVI < 1.0$ and $0 < f_{IPAR} < 0.95$). The f_T is the plant temperature constraint, T_{max} is the maximum air temperature, T_{opt} is the optimum plant growth temperature and $\lambda = T_{opt}$, and R_{nc} is net radiation to the canopy.

The interception evaporation (ET_i) can be described as follows:

$$ET_i = f_{wet}\alpha\frac{\Delta}{\Delta + \gamma}R_{nc}, \tag{14}$$

3.2. Trend Analysis

We used significance testing and trend analysis to explore the spatiotemporal characteristics of ET in the CONUS from 2001 to 2022, both annually and seasonally, in order to better understand ET's spatiotemporal characteristics in the CONUS and explore its variation patterns.

Trend analysis is used to analyze the temporal changes of variables such as *ET*, *NDVI*, T_a, and *P* in the CONUS from 2001 to 2022. In this study, a linear regression trend analysis was performed using the least squares method, as follows:

$$y = s \times x + i, \tag{15}$$

$$s = \frac{n \times \sum_{i=1}^{n} i \times x_i - \sum_{i=1}^{n} i \sum_{i=1}^{n} x_i}{n \times \sum_{i=1}^{n} i^2 - \left(\sum_{i=1}^{n} i\right)^2}, \tag{16}$$

where *s* is the slope, which is the interannual change rate of the variable, *i* represents the year, and *n* equals 22, representing the number of years used to calculate the slope. x_i is the variable value for the *i-th* year. When *s* is greater than 0, the variable *x* shows an increasing trend; when *s* is less than 0, the variable *x* shows a downward trend.

The significance test is used to test whether the trend of change in variables (slope *s*) is significant. The student *t*-test was used in this study. When the significance *p*-value is less than 0.05, the trend is significant at the 95% confidence level.

4. Results

### 4.1. Evaluation of PT-SinRH for Estimating ET at Site Scale

To evaluate the accuracy of the PT-SinRH simulations driven by satellite and reanalysis data, a statistical comparison of the ET estimates and observations from 28 AmeriFlux sites (Table 1) reveals that the daily ET estimated by the PT-SinRH model exhibits KGE values ranging from 0.22 to 0.66 and an R^2 varies between 0.28 and 0.77, while the RMSE varies between 6.0 and 33.5 W/m^2, and the values of bias varies between -28.3 and 14.3 W/m^2. For all sites, the PT-SinRH model demonstrated its best performance in reproducing ET at US-MWA, achieving satisfactory accuracy with an R^2 of 0.6, a KGE of 0.65, a bias of

1.0 W/m^2, and an RMSE of 12.1 W/m^2. In contrast, the accuracy of the PT-SinRH model at US-Rws was significantly poorer, with a minimum KGE of 0.22.

Table 1. Comparison of the predicted ET based on the PT-SinRH model driven by satellite and reanalysis data inputs and daily observed ET for all 28 sites.

IGBP	Site Name	R^2	RMSE (W/m^2)	Bias (W/m^2)	KGE
CRO	US-Bi1	0.69	32.8	−26.7	0.35
	US-IB1	0.33	23.2	−13.8	0.34
	US-KL1	0.54	15.6	−7.3	0.58
	US-KM1	0.47	15.6	−5.7	0.59
	US-MWA	0.60	12.1	1.0	0.65
	US-Ro6	0.49	12.8	−4.7	0.56
	US-Tw3	0.72	33.5	−28.0	0.37
GRA	US-AR1	0.65	19.4	9.7	0.53
	US-Snf	0.71	31.9	−28.3	0.41
	US-Var	0.77	26.1	−22.3	0.43
	US-xAE	0.61	15.0	6.6	0.54
	US-xCL	0.53	22.9	14.3	0.46
	US-xKA	0.44	18.2	−8.1	0.47
DBF	US-CMW	0.39	6.0	−3.5	0.29
	US-Slt	0.49	17.8	2.8	0.49
	US-Wpp	0.65	15.8	−10.4	0.59
	US-xBL	0.59	13.2	−2.8	0.66
ENF	US-Me6	0.28	17.2	4.7	0.41
	US-xAB	0.51	20.2	−13.3	0.48
	US-xJE	0.46	23.5	4.7	0.66
	US-xTA	0.41	25.1	7.7	0.43
WET	US-MWW	0.52	15.7	1.1	0.57
	US-Myb	0.51	28.7	−19.2	0.4
	US-ORv	0.58	13.2	0.8	0.47
	US-WPT	0.52	20.2	−13.4	0.44
SHR	US-Rws	0.37	19.8	−15.7	0.22
	US-Ton	0.70	19.0	−12.9	0.49
MF	US-xDL	0.40	24.8	10.6	0.48

Furthermore, we conducted site validation for the PT-SinRH model on a daily scale and Figure 2 illustrates the precision of daily ET estimates based on the PT-SinRH under various land cover types. The findings reveal that the estimated ET of the PT-SinRH model is comparable to the observed ET, and the PT-SinRH demonstrates a certain level of simulation performance. In comparison, the PT-SinRH model has the ex-cellent performance in evergreen needleleaf forest (ENF), with an average R^2 of 0.58, KGE of 0.70, and RMSE of 15.2 W/m^2, a bias of 2.4 W/m^2. However, the PT-SinRH model has the worst performance in cropland (CRO), with an average KGE of only 0.40. Specifically, for all sites, the R^2 value is 0.50, the RMSE is 16.0 W/m^2, the bias is −2.0 W/m^2, and the KGE is 0.70. At the same time, due to the better performance of PT-JPL compared to other ET models [36], the PT-JPL model was chosen for comparison with the observations, as displayed in Figure 2. Then, compared with the PT-JPL, the PT-SinRH model enhances the precision of estimated ET values, improving the KGE and R^2 values by 0.01 and reducing RMSE by approximately 0.2 W/m^2.
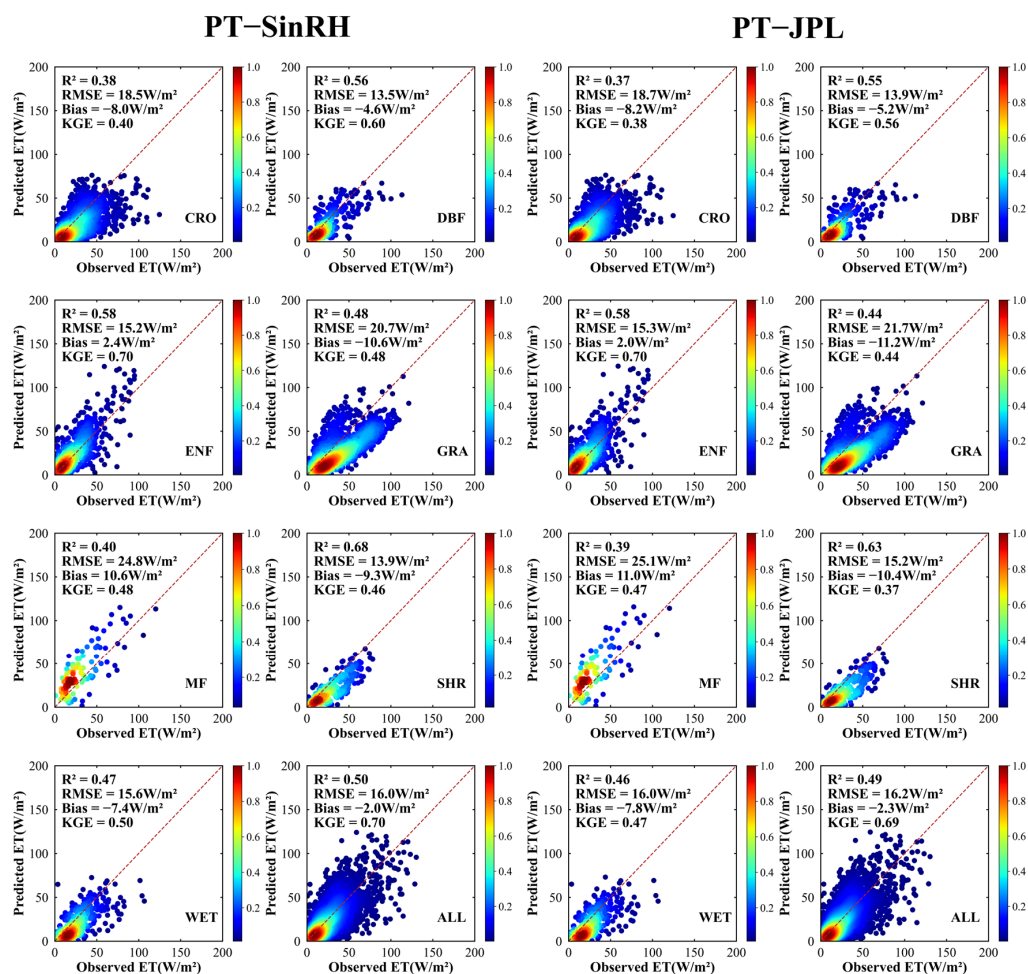
Figure 2. Scatterplots of predicted ET and daily observed ET based on satellite and reanalysis data input at various land cover types.

4.2. Mean Spatial Pattern of ET over the CONUS

4.2.1. Annual

The spatial distribution of ET averaged across the CONUS from 2001 to 2022 (Figure 3) exhibits significant spatial heterogeneity, and the distribution manifests a high-low-high pattern extending from the western to the eastern regions, attributing to the influence of subsurface characteristics and climatic factors. The estimations of ET based on the PT-SinRH model had an annual mean of 42.54 W/m^2 from 2001 to 2022 in CONUS. Using the Mississippi River as a boundary, the CONUS is divided into east and west regions. ET in the mountainous regions of the west is relatively low, ranging from 0 to 50 W/m^2. This area receives minimal precipitation and is characterized by a relatively arid climate. In this region, ET is higher in the lower-elevation woodlands located in the northern areas compared to the higher-elevation grasslands found in the southern areas. It is worth noting that ET is higher along the west coast near the Pacific Ocean. The southern and southeastern regions have subtropical monsoon humid climates, heavily influenced by the Gulf of Mexico Warm Current. These areas receive ample precipitation and exhibit high ET. The highest value occurs in the southeastern United States, exceeding 100 W/m^2.
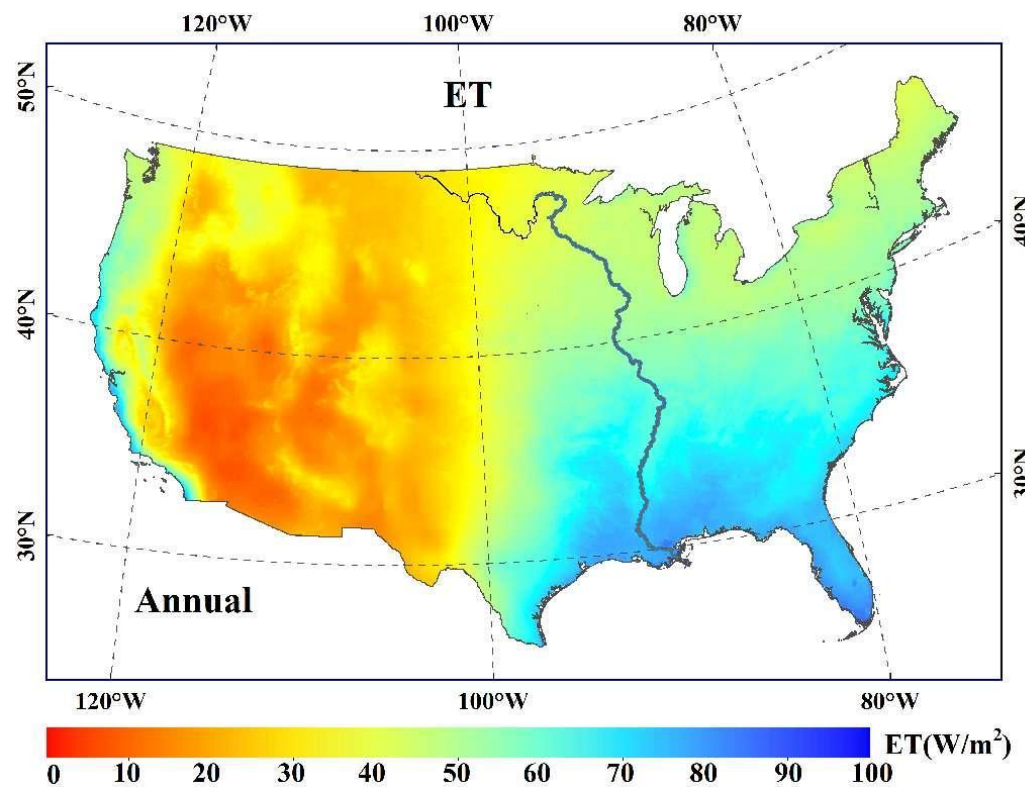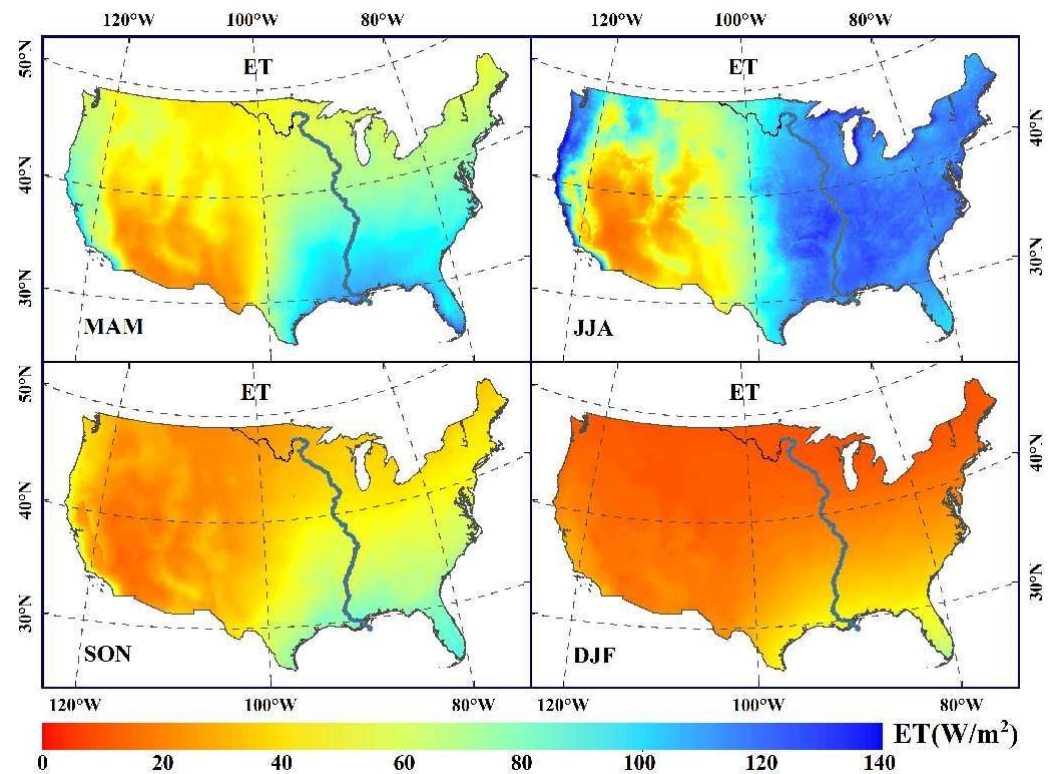
Figure 3. Annual spatial patterns of ET over the CONUS during 2001–2022.

4.2.2. Seasonal

The spatial distribution of ET in different seasons showed a significant difference (Figure 4). The spatial distribution patterns of ET during MAM (March, April, and May) and SON (September, October, and November) closely resemble the annual average distribution pattern and generally exhibit variations corresponding to the altitude of the study area. The western coastal area has higher ET, while the western inland area has lower ET, less than 60 W/m^2. ET in the eastern region is substantial, exhibiting a gradient that decreases from south to north.

During the JJA (June, July, and August), there are significant differences between the western and eastern regions. The west coast region, along with the eastern region, is characterized by lower altitudes and proximity to the sea. These regions experience ample rainfall and a humid climate, resulting in ET rates exceeding 100 W/m^2. However, the western mountains are landlocked at higher altitudes, with a dry climate and less ET. The spatial heterogeneity of land surface ET is the highest during this season. In DJF (December, January, and February), ET is low throughout the region, and the effect of temperature is significant. The ET shows a decreasing distribution pattern from south to north. In general, the spatial distribution of ET in the CONUS during different seasons is related to elevation and climate type.

Figure 4. Seasonal spatial patterns of ET over the CONUS from 2001 to 2022. MAM (spring): March, April, and May; JJA (summer): June, July, and August; SON (Fall): September, October, and November; DJF (Winter): December, January, and February.

4.3. Temporal Characteristics of ET Trends over the CONUS

4.3.1. Annual

Figure 5 shows that the ET estimations of CONUS based on the PT-SinRH model increased from 2001 to 2022 with a linear fit having a slope of 0.76 $W/m^2/da$ ($p < 0.05$). Considering the different climatic and hydrological conditions in the east and west of the CONUS, the trend of ET in the west and east of the CONUS was further calculated. The growing tendency of ET in the east of CONUS became more obvious, which appears to drive ET increase across the CONUS. During the years between 2001 and 2022, the annual ET of the west of CONUS exhibited a rate of increase at 0.42 $W/m^2/da$ ($p < 0.05$), while the annual ET of the east of CONUS exhibited a rate of increase at 1.45 $W/m^2/da$ ($p < 0.05$).
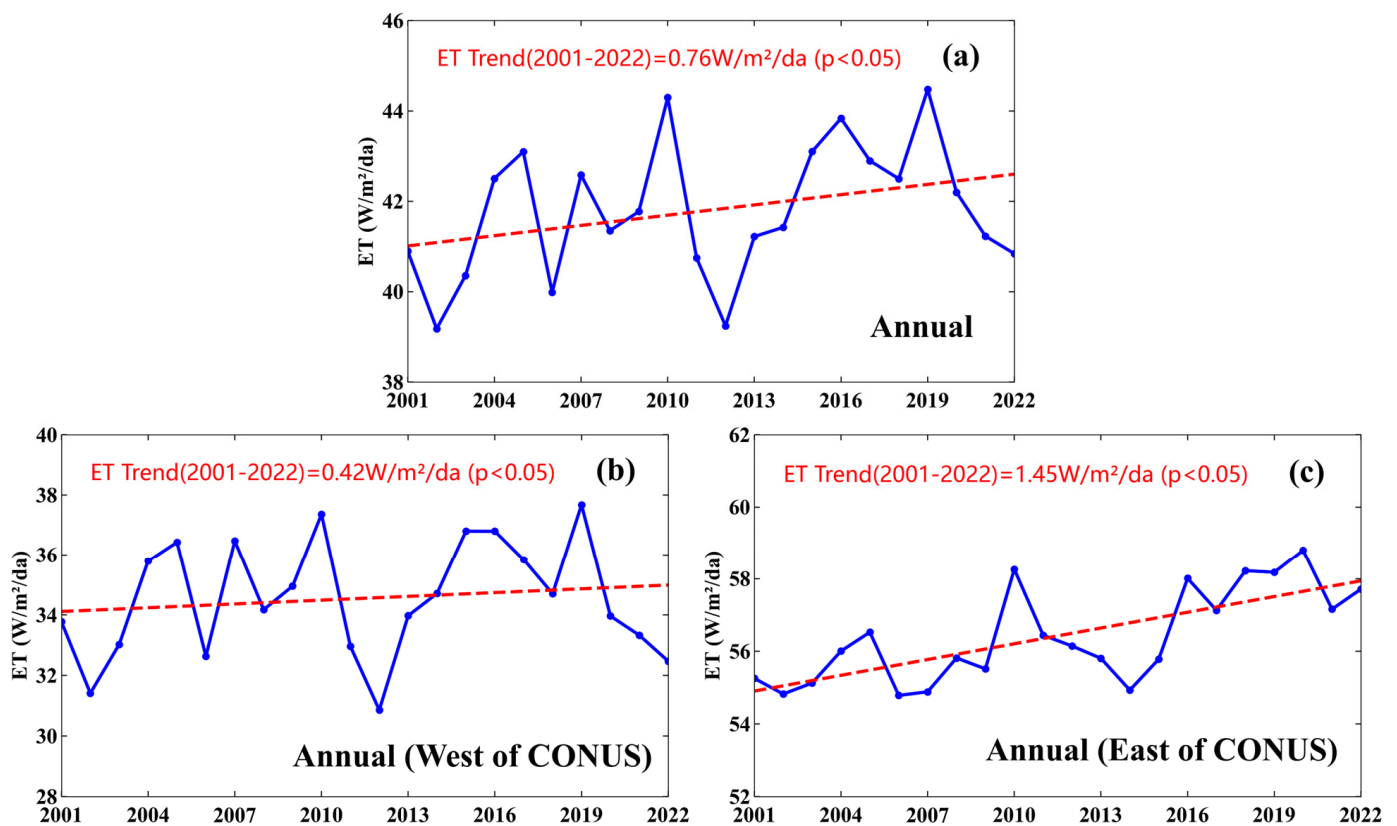
Figure 5. Interannual variability of ET from 2001 to 2022 over the (**a**) CONUS, (**b**) west of CONUS, and (**c**) east of CONUS.

4.3.2. Seasonal

We plotted the interannual seasonal variability of ET over the CONUS estimated by PT-SinRH for the four seasons, including MAM, JJA, SON, and DJF. Figure 6 shows that ET increases at a rate of 2.67, 0.32, and 0.15 $W/m^2/da$ ($p < 0.05$) for JJA, SON, and DJF, respectively, but there was a rate of decrease at 0.11 $W/m^2/da$ ($p < 0.05$) for MAM over the CONUS from 2001 to 2022. The unexpected decrease was influenced by the decline of ET for MAM in the west of CONUS, which exhibited a rate of decrease at 0.21 $W/m^2/da$ ($p < 0.05$) from 2001 to 2022. The seasonal comparison of ET trends during the study period indicates that the magnitude of the ET increase during JJA is significantly higher than that of SON and DJF, which has reached 3.5 times the annual increase of ET over the CONUS. Moreover, the regional comparison of ET trends indicates that the obvious increase of ET trend diagnosed during JJA occurred primarily in the east of CONUS, and it exhibited a rate of increase at 4.24 $W/m^2/da$ ($p < 0.05$). The ET trend of interannual seasonal changes in the east of CONUS has always maintained and increased even during MAM, whereas those in the west of CONUS are more stable, with a slight negative growth during MAM and DJF and a growth rate of only 1.89 $W/m^2/da$ ($p < 0.05$) during JJA. The difference in the seasonal contribution of eastern and western ET patterns to the CONUS agrees with the annual contribution. These interannual variability indicate that the growing tendency of ET over CONUS from 2001 to 2022 was mainly driven by changes in the summer seasons in the eastern.
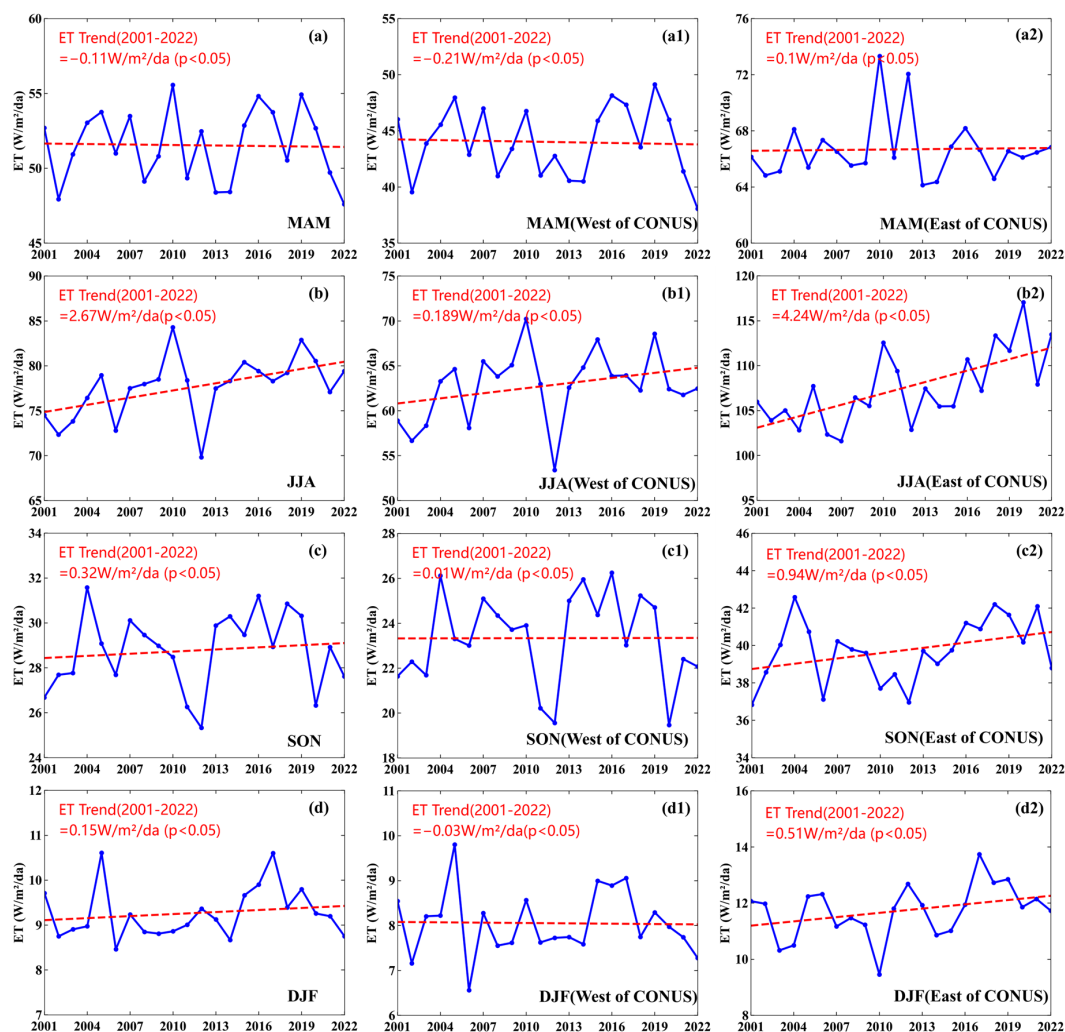
Figure 6. Interannual seasonal variability of ET from 2001 to 2022 over the CONUS [(**a**) MAM, (**b**) JJA, (**c**) SON, and (**d**) DJF], west of CONUS [(**a1**) MAM, (**b1**) JJA, (**c1**) SON, and (**d1**) DJF], and east of CONUS [(**a2**) MAM, (**b2**) JJA, (**c2**) SON, and (**d2**) DJF].

4.4. Spatial Patterns of ET Trends Changes over the CONUS

4.4.1. Annual

Figure 7 illustrates the annual spatiotemporal variations of ET trends estimated by the PT-SinRH model over the CONUS from 2001 to 2022. The ET of the CONUS showed an increasing trend in most regions, and more than 80% of the regions passed the significance test of $p < 0.05$. The increase of ET in space mainly occurred in the eastern region of the CONUS, with an increase rate of about 6–8 W/m^2/da. The ET of forests and grasslands in the western region of the CONUS also showed a large increase rate. The ET in the western region of the CONUS has significantly decreased from 2001 to 2022, especially in the coastal areas where the reduction rate exceeded 10 W/m^2/da. The ET of shrublands in the southwestern of CONUS also showed a significant decrease.
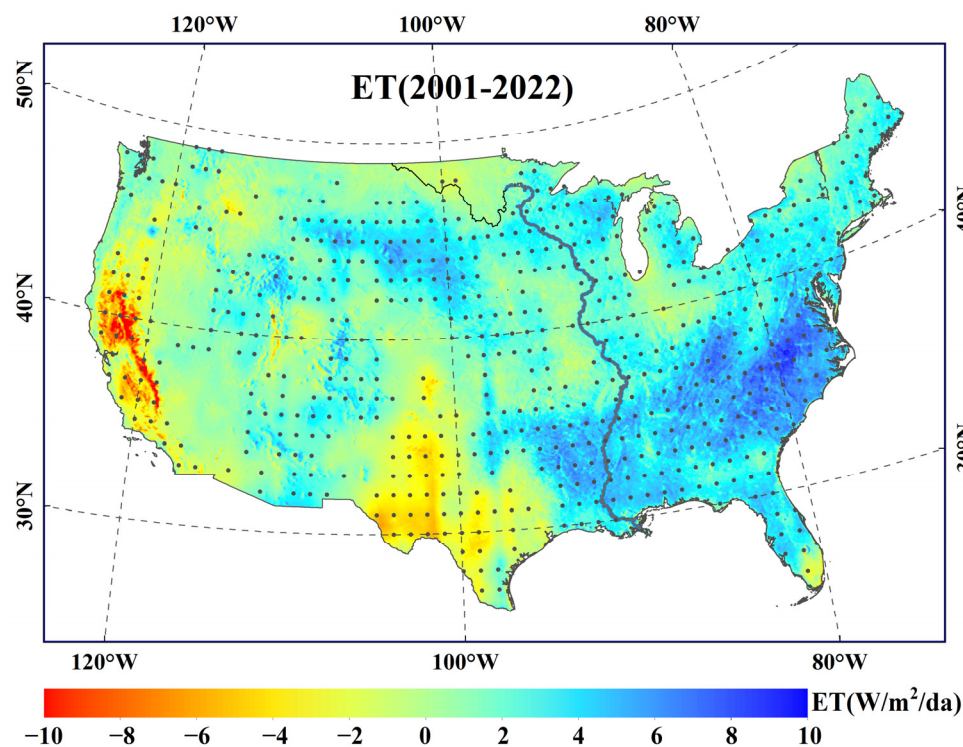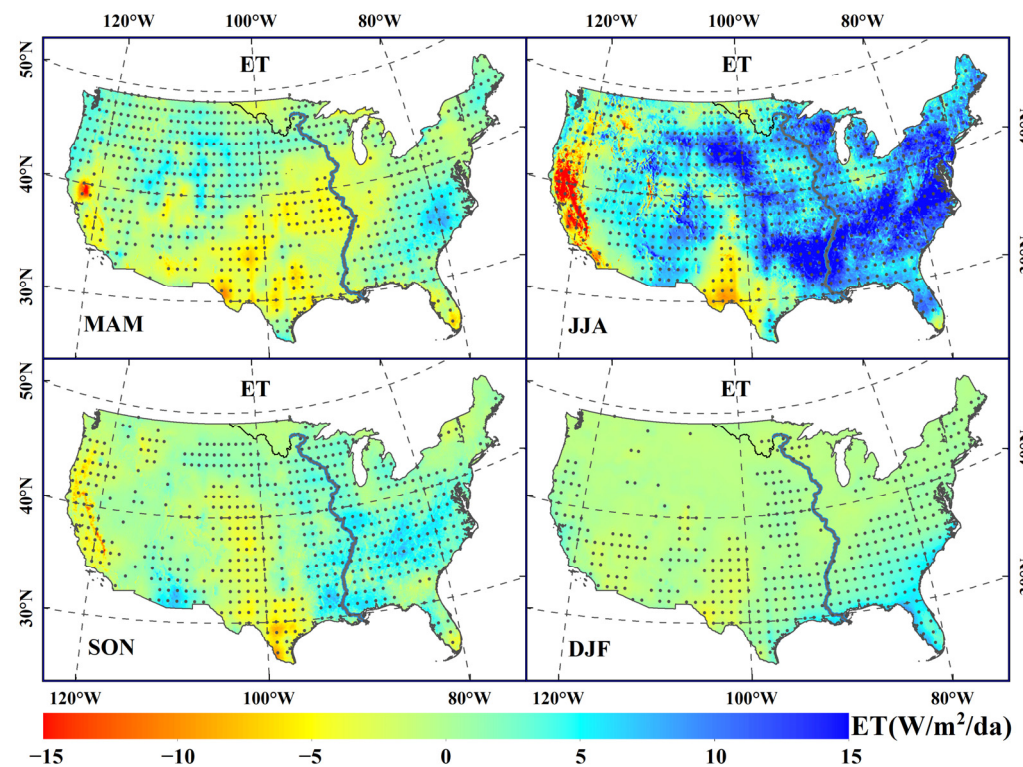
Figure 7. Annual spatiotemporal variations of ET over the CONUS from 2001 to 2022 ($p < 0.05$). Black dots mean the regions have been checked by significant tests at a 95% confidence level.

4.4.2. Seasonal

Figure 8 presents the multiyear (2001–2022) seasonal spatiotemporal variations of ET trends across the CONUS. As depicted in Figure 8, the distribution of interannual ET variation trend exhibits distinct seasonal patterns. During the MAM and SON, the CONUS has shown mild changes from 2001 to 2022. The seasonal variations of ET for MAM and SON are usually between -5 and 5 W/m^2/da, and more than 70% of the CONUS have passed the significance test with $p < 0.05$. The interannual variability of ET in JJA is more pronounced than that of MAM and SON. More than 80% of CONUS show an increase in ET, with a seasonal variation of up to 15 W/m^2/da. In the western coastal areas of the CONUS, ET is decreasing with a seasonal variation of 15 W/m^2/da. Most regions exhibit a seasonal variation of around 5 W/m^2/da, and over 95% of the CONUS have passed a significance test with $p < 0.05$. In the DJF, ET changes are minimal, with a slight increase observed in the southeastern coastal areas, while most regions exhibit changes close to 0 W/m^2/da. Therefore, the variation in the ET trend in JJA could constitute the majority of the changes in the aggregate annual ET trend.

Furthermore, we observed distinct regional distribution patterns in the Northeast. For instance, during MAM, the peak ET is concentrated in the eastern part of this region. However, in the JJA, the ET peak expands and shifts westward. Previous research [31] has indicated that in JJA, due to abundant solar radiation, increasing temperatures, and vigorous vegetation transpiration, forest ecosystems exhibit higher ET intensity compared to other ecosystems. Figure 8 depicts regions with high ET values predominantly located in the eastern and central parts, where forests are densely populated. This suggests that the distribution of forests significantly influences the ET distribution characteristics during the JJA. As the rainy season concludes and temperatures decline, ET gradually diminishes from SON to DJF.

Figure 8. Seasonal spatiotemporal variations of ET over the CONUS from 2001 to 2022. Black dots mean the regions have been checked by significant tests at a 95% confidence level.

5. Discussion

5.1. Variation in ET Trends Change over the CONUS

In this study, the spatial distribution of annual and seasonal ET variations increase from west to east (Figures 3 and 4), and the interannual variations of ET estimates increase significantly over most regions of the CONUS, including the eastern and western CONUS (Figures 7 and 8), which are accord with the previous studies [43,44], and further, prove that the PT-SinRH model can simulate the spatiotemporal variations of ET over the CONUS. ET trends vary among the seasons and regions, and the increasing ET over the eastern CONUS in summer contributed the most increment (Figure 6). They are closely regulated by the available local water and energy [45]. For example, atmospheric situations lead to increased ET with limited energy in humid climates [46]. The water-limited and warm climates with positive ET anomalies may cause drought [47].

Most previous studies found that the water constraint (i.e., *P*) was significant reason for ET variations [29,30]. The ET spatial patterns rise from west to east over the CONUS at the annual scale (Figure 3) due to the increase of precipitation from west to east (Figure 9). The spatial variations of precipitation are consistent with that of ET at an annual scale. The significantly increasing trend of annual precipitation may result in the ET increasing variations. The increasing rate of annual precipitation over the east of CONUS is greater than that over the west of CONUS (Figures 10 and 11), which is consistent with the differences in ET increasing rates between the western and eastern CONUS (Figures 5 and 7). Over the eastern CONUS, the ET increased significantly from 2001 to 2022 (Figure 5) because of the precipitation increasing over this region at an annual scale (Figure 10). These results can prove that precipitation is a dominant factor in ET variations. In addition, NDVI is also another forcing factor of ET dynamics. NDVI increases from west to east, consistent with ET spatial variations (Figures 3 and 9). From 2001 to 2022, NDVI increased significantly with a rate of 0.01 (*p* < 0.05). The increasing trend of NDVI over the eastern CONUS is obviously higher than the western, which is consistent with the trend differences in the

precipitation and ET (Figures 5, 7, 10 and 11). Vegetation greening with increasing NDVI and precipitation variations leads to ET increasing over the CONUS [48].
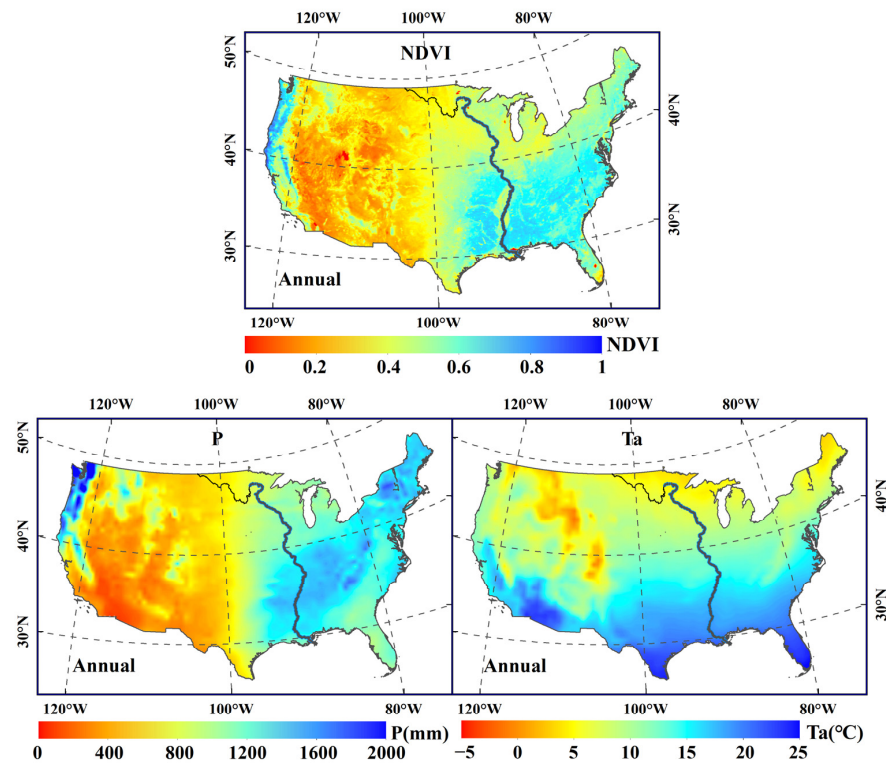
Figure 9. Annual spatial patterns of NDVI, precipitation (P), and temperature (Ta) over the CONUS from 2001 to 2022.
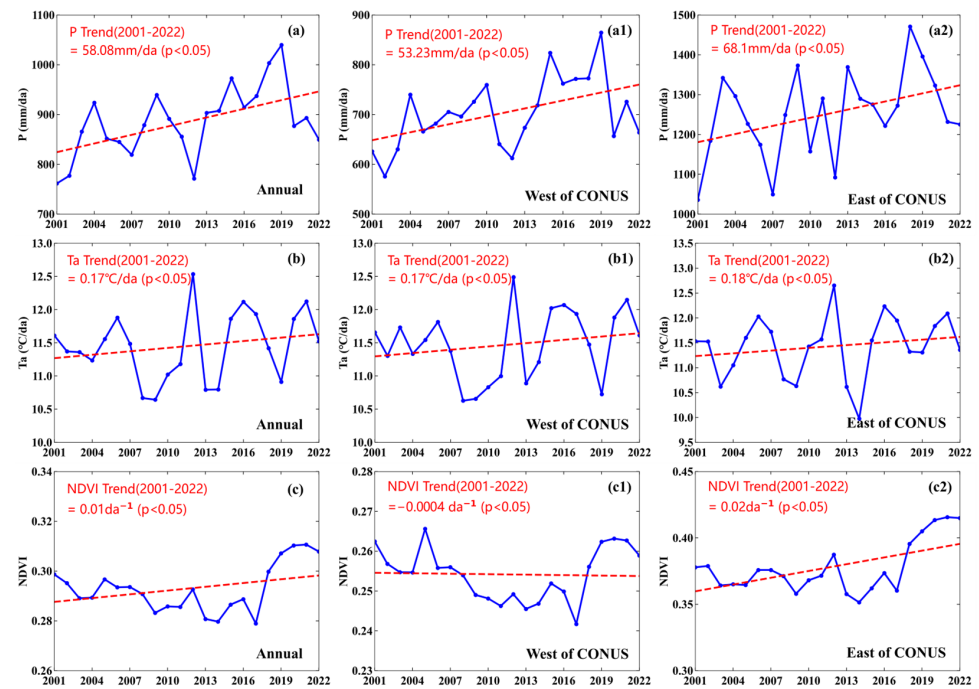
Figure 10. Annual temporal variations of precipitation (P), temperature (Ta), and NDVI over the CONUS [(**a**–**c**)], west of CONUS [(**a1**–**c1**)], and east of CONUS [(**a2**–**c2**)] from 2001 to 2022.
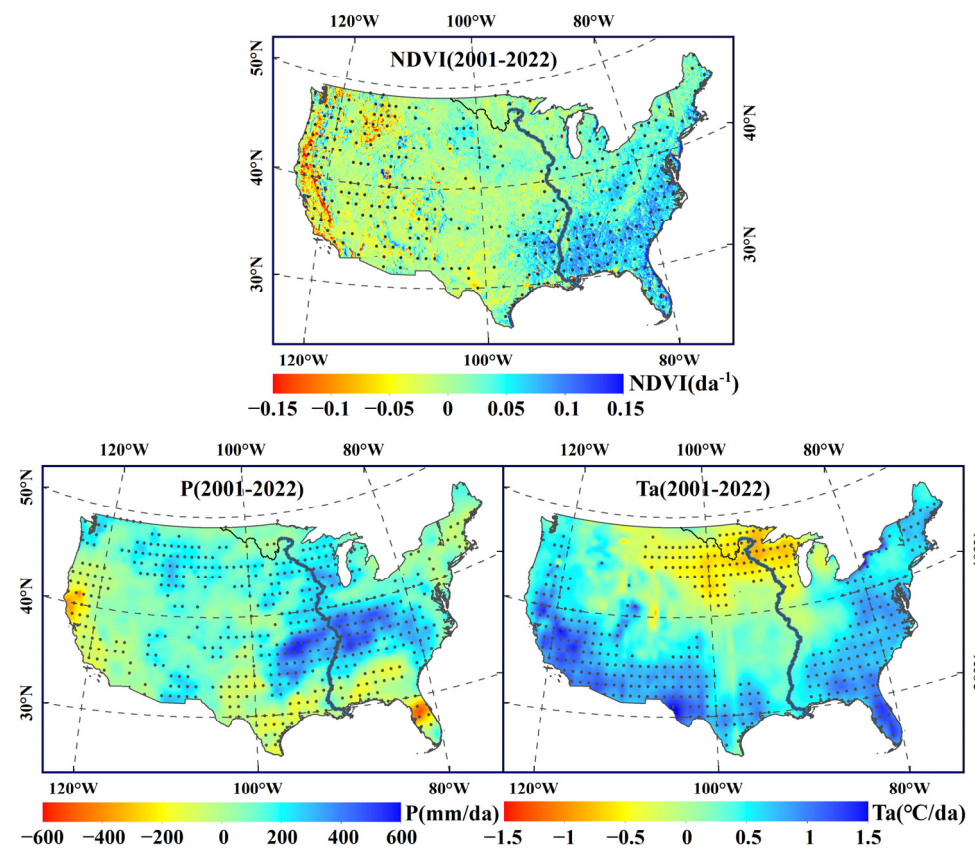
Figure 11. Annual spatiotemporal variations of NDVI, precipitation (P), and temperature (T_a) over the CONUS from 2001 to 2022. Black dots mean the regions have been checked by significant tests at a 95% confidence level.

ET annual variations and anomalies can reflect climate extremes such as extreme drought and precipitation [49,50]. Prior studies found that the southwestern CONUS had been influenced by El Niño-Southern Oscillation (ENSO) based on GLEAM and FLUXNET data [51,52]. Because La Nina occurred in 2012, compared to the multiyear means of climate variables, the temperature increased, but precipitation decreased over the central and western CONUS. These lead to droughts with decreasing ET over those regions (Figure 12). Previous studies found that serious flash droughts were often connected with La Niña, the positive-phase American Multidecadal Oscillation, or the negative-phase Pacific Decadal Oscillation over most CONUS regions [53]. ENSO may cause global variations of atmosphere-land water flux, water cycle, and extreme climate events [34].

The ET spatiotemporal variations also have several uncertainties. The input data in this study include GLASS and MERRA-2 data with different spatial resolutions, which causes large uncertainties. Compared with the ET observations, the estimates of PT-SinRH have uncertainties with a bias of -8.6 W/m^2 and an RMSE of 20.3 W/m^2 (Figure 2). The uncertainties of PT-SinRH estimates may also be sent to the ET spatiotemporal variations.
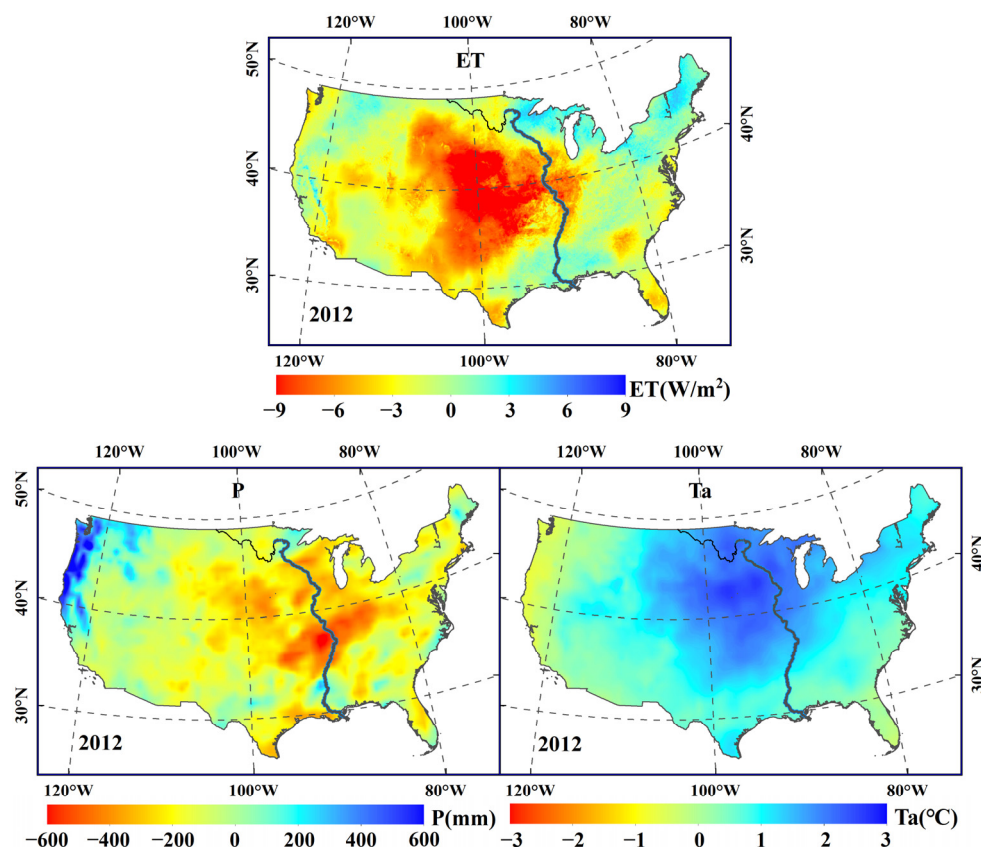
Figure 12. Evapotranspiration (ET), precipitation (P), and temperature (Ta) anomalies over the CONUS on 2012.

5.2. Implications for Large-Scale Hydrometeorological Change

Due to the lack of high spatiotemporal ET products in CONUS, we generated the daily ET products with a 0.05° spatial resolution based on the PT-SinRH model from 2001 to 2022. Accurate estimation of ET datasets is essential for indirect assessment of the coarse-resolution ET products and monitoring of field water resources [54]. Additionally, ET datasets can provide an invaluable resource for measuring ecological and hydrological reactions to climatic changes and agricultural water management [27,52,55]. Furthermore, ET datasets present a chance to investigate the mechanisms governing ET in these areas in the future [56]. Therefore, the accurate ET dataset is significant for decision-making support for global climate change, forest ecosystems, and regional agricultural drought. An accurate estimation of forest ET can not only protect and maintain the healthy and sustainable development of forest ecosystems but also enrich the species diversity within forest ecosystems and promote the development of global ecosystems and human society.

We found that the ET dataset based on PT-SinRH in CONUS showed an increasing trend from 2001 to 2022, which could be considerably impacted by the increasing precipitation, Ta, and NDVI. Our results are consistent with recent research by Yang et al. [57], who reported an increasing trend in global ET from 1982 to 2011, and the authors attribute this phenomenon to vegetation greening and increased precipitation [57]. Moreover, ET has received increasing attention as a critical indicator for better understanding the water cycles, ecosystem carbon and coupling mechanisms, which is important in response to drought [58,59].

6. Conclusions

The main objective of this study is to estimate ET in CONUS from 2001 to 2022 based on the PT-SinRH model. After verifying the reliability of the PT-SinRH model at the site scale by using the observed ET data of 28 EC sites, we analyzed the spatiotemporal

characteristics of ET from 2001 to 2022 by using satellite and meteorological reanalysis data. The results demonstrate that the PT-SinRH model was effective in calculating ET over CONUS. The main conclusions of the study are as follows:

(1) The PT-SinRH model yielded superior performance at 28 EC sites, and the RMSE varies from 6.0 to 33.5 W/m^2, the KGE varies from 0.22 to 0.66.

(2) The ET calculated based on the PT-SinRH model has an annual mean of 42.54 W/m^2 from 2001 to 2022 in CONUS, and the spatial patterns of annual and seasonal ET variations increase from west to east.

(3) The ET in the CONUS from 2001 to 2022 exhibits both seasonal and annual linear trends, with an average increase of 0.76 $W/m^2/da$ ($p < 0.05$).

(4) The change of P and NDVI plays a major controlling influence on the change of ET over CONUS.

Therefore, accurate ET estimates have great importance for forest ecosystems and regional agricultural drought research and can also provide a scientific foundation for managing water resource, conserving forest, responding to climate change, and other aspects. By strengthening monitoring network construction and science popularization education strategies, important references are provided for achieving more scientific and rational forest management and water resource utilization.

Author Contributions: Conceptualization, L.L. and Y.Y.; methodology, L.L. and Y.Y; software, L.L. and R.Y.; validation, Z.X. and J.N.; formal analysis, L.L.; investigation, J.F. and L.Z.; resources, Y.K. and J.X.; data curation, L.L.; writing—original draft preparation, L.L.; writing—review and editing, Y.Y. and Y.L.; visualization, L.L.; funding acquisition, Y.Y. All authors have read and agreed to the published version of the manuscript.

Data Availability Statement: The data presented in this study are available on request from the corresponding author. The data are not publicly available due to privacy.

Conflicts of Interest: The authors declare no conflicts of interest.

References

1. Thornthwaite, C.W. An Approach toward a Rational Classification of Climate. *Geogr. Rev.* **1948**, *38*, 55–94.
2. Monteith, J.I.L. Evaporation and Environment. *Symp. Soc. Exp. Biol.* **1965**, *19*, 205–234.
3. Fisher, J.B.; Melton, F.; Middleton, E.; Hain, C.; Anderson, M.; Allen, R.; McCabe, M.F.; Hook, S.; Baldocchi, D.; Townsend, P.A.; et al. The future of evapotranspiration: Global requirements for ecosystem functioning, carbon and climate feedbacks, agricultural management, and water resources. *Water Resour. Res.* **2017**, *53*, 2618–2626.
4. Vicente-Serrano, S.M.; Beguería, S.; López-Moreno, J.I. A Multiscalar Drought Index Sensitive to Global Warming: The Standardized Precipitation Evapotranspiration Index. *J. Clim.* **2010**, *23*, 1696–1718.
5. Tian, H.; Chen, G.; Liu, M.; Zhang, C.; Sun, G.; Lu, C.; Xu, X.; Ren, W.; Pan, S.; Chappelka, A. Model estimates of net primary productivity, evapotranspiration, and water use efficiency in the terrestrial ecosystems of the southern United States during 1895–2007. *For. Ecol. Manag.* **2010**, *259*, 1311–1327.
6. Valipour, M.; Sefidkouhi, M.A.G.; Raeini−Sarjaz, M. Selecting the best model to estimate potential evapotranspiration with respect to climate change and magnitudes of extreme events. *Agric. Water Manag.* **2017**, *180*, 50–60.
7. Wang, K.; Dickinson, R.E.; Wild, M.; Liang, S. Evidence for decadal variation in global terrestrial evapotranspiration between 1982 and 2002: 2. Results. *J. Geophys. Res. Atmos.* **2010**, *115*, D20113.
8. Kukal, M.; Irmak, S. Long-term patterns of air temperatures, daily temperature range, precipitation, grass-reference evapotranspiration and aridity index in the USA great plains: Part II. Temporal trends. *J. Hydrol.* **2016**, *542*, 978–1001.
9. Jung, M.; Reichstein, M.; Ciais, P.; Seneviratne, S.I.; Sheffield, J.; Goulden, M.L.; Bonan, G.; Cescatti, A.; Chen, J.; de Jeu, R.; et al. Recent decline in the global land evapotranspiration trend due to limited moisture supply. *Nature* **2010**, *467*, 951–954.
10. Jung, M.; Reichstein, M.; Margolis, H.A.; Cescatti, A.; Richardson, A.D.; Arain, M.A.; Arneth, A.; Bernhofer, C.; Bonal, D.; Chen, J.; et al. Global patterns of land-atmosphere fluxes of carbon dioxide, latent heat, and sensible heat derived from eddy covariance, satellite, and meteorological observations. *J. Geophys. Res.* **2011**, *116*, G00J07.
11. Xu, T.; Guo, Z.; Liu, S.; He, X.; Meng, Y.; Xu, Z.; Xia, Y.; Xiao, J.; Zhang, Y.; Ma, Y.; et al. Evaluating Different Machine Learning Methods for Upscaling Evapotranspiration from Flux Towers to the Regional Scale. *J. Geophys. Res. Atmos.* **2018**, *123*, 8674–8690.

12. Wang, K.; Liang, S. An Improved Method for Estimating Global Evapotranspiration Based on Satellite Determination of Surface Net Radiation, Vegetation Index, Temperature, and Soil Moisture. *J. Hydrometeorol.* **2008**, *9*, 712–727.

13. Wang, K.; Dickinson, R.E.; Wild, M.; Liang, S. Evidence for decadal variation in global terrestrial evapotranspiration between 1982 and 2002: 1. Model development. *J. Geophys. Res.* **2010**, *115*, D20112.

14. Zhu, W.; Jia, S.; Lv, A. A UniversalTs-VI Triangle Method for the Continuous Retrieval of Evaporative Fraction From MODIS Products. *J. Geophys. Res. Atmos.* **2017**, *122*, 10206–10227.

15. Carrera, M.L.; Bélair, S.; Bilodeau, B. The Canadian Land Data Assimilation System (CaLDAS): Description and Synthetic Evaluation Study. *J. Hydrometeorol.* **2015**, *16*, 1293–1314.

16. Xia, Y.; Hao, Z.; Shi, C.; Li, Y.; Meng, J.; Xu, T.; Wu, X.; Zhang, B. Regional and Global Land Data Assimilation Systems: Innovations, Challenges, and Prospects. *J. Meteorol. Res.* **2019**, *33*, 159–189.

17. Xu, T.; Liu, S.; Liang, S.; Qin, J. Improving Predictions of Water and Heat Fluxes by Assimilating MODIS Land Surface Temperature Products into the Common Land Model. *J. Hydrometeorol.* **2011**, *12*, 227–244.

18. Zhang, B.; Xia, Y.; Long, B.; Hobbins, M.; Zhao, X.; Hain, C.; Li, Y.; Anderson, M.C. Evaluation and comparison of multiple evapotranspiration data models over the contiguous United States: Implications for the next phase of NLDAS (NLDAS-Testbed) development. *Agric. For. Meteorol.* **2020**, *280*, 107810.

19. Jia, Z.; Liu, S.; Mao, D.; Wang, Z.; Xu, Z.; Zhang, R. A Study of the Validation Method of Remotely Sensed Evapotranspiration based on Observation Data. *Adv. Earth Sci.* **2010**, *25*, 1248–1260.

20. Mu, Q.; Heinsch, F.A.; Zhao, M.; Running, S.W. Development of a global evapotranspiration algorithm based on MODIS and global meteorology data. *Remote Sens. Environ.* **2007**, *111*, 519–536.

21. Mu, Q.; Zhao, M.; Running, S.W. Improvements to a MODIS global terrestrial evapotranspiration algorithm. *Remote Sens. Environ.* **2011**, *115*, 1781–1800.

22. Senay, G.B.; Bohms, S.; Singh, R.K.; Gowda, P.H.; Velpuri, N.M.; Alemu, H.; Verdin, J.P. Operational Evapotranspiration Mapping Using Remote Sensing and Weather Datasets: A New Parameterization for the SSEB Approach. *Jawra J. Am. Water Resour. Assoc.* **2013**, *49*, 577–591.

23. Yao, Y.; Liang, S.; Li, X.; Hong, Y.; Fisher, J.B.; Zhang, N.; Chen, J.; Cheng, J.; Zhao, S.; Zhang, X.; et al. Bayesian multimodel estimation of global terrestrial latent heat flux from eddy covariance, meteorological, and satellite observations. *J. Geophys. Res. Atmos.* **2014**, *119*, 4521–4545.

24. Martens, B.; Miralles, D.; Lievens, H.; Fernández-Prieto, D.; Verhoest, N.E.C. Improving terrestrial evaporation estimates over continental Australia through assimilation of SMOS soil moisture. *Int. J. Appl. Earth Obs. Geoinf.* **2016**, *48*, 146–162.

25. Martens, B.; Miralles, D.G.; Lievens, H.; Schalie, R.; de Jeu, R.A.M.; Fernández-Prieto, D.; Beck, H.E.; Dorigo, W.A.; Verhoest, N.E.C. GLEAM v3: Satellite-based land evaporation and root-zone soil moisture. *Geosci. Model Dev.* **2017**, *10*, 1903–1925.

26. Long, D.; Longuevergne, L.; Scanlon, B.R. Uncertainty in evapotranspiration from land surface modeling, remote sensing, and GRACE satellites. *Water Resour. Res.* **2014**, *50*, 1131–1151.

27. Xu, T.; Guo, Z.; Xia, Y.; Ferreira, V.G.; Liu, S.; Wang, K.; Yao, Y.; Zhang, X.; Zhao, C. Evaluation of twelve evapotranspiration products from machine learning, remote sensing and land surface models over conterminous United States. *J. Hydrol.* **2019**, *578*, 124105.

28. Velpuri, N.M.; Senay, G.B. Partitioning Evapotranspiration into Green and Blue Water Sources in the Conterminous United States. *Sci. Rep.* **2017**, *7*, 6191.

29. Chen, Y.; Xia, J.; Liang, S.; Feng, J.; Fisher, J.B.; Li, X.; Li, X.; Liu, S.; Ma, Z.; Miyata, A.; et al. Comparison of satellite-based evapotranspiration models over terrestrial ecosystems in China. *Remote Sens. Environ.* **2014**, *140*, 279–293.

30. McVicar, T.R.; Roderick, M.L.; Donohue, R.J.; Li, L.T.; Van Niel, T.G.; Thomas, A.; Grieser, J.; Jhajharia, D.; Himri, Y.; Mahowald, N.M.; et al. Global review and synthesis of trends in observed terrestrial near-surface wind speeds: Implications for evaporation. *J. Hydrol.* **2012**, *416–417*, 182–205.

31. Mo, X.; Liu, S.; Lin, Z.; Wang, S.; Hu, S. Trends in land surface evapotranspiration across China with remotely sensed NDVI and climatological data for 1981–2010. *Hydrol. Sci. J.* **2015**, *60*, 2163–2177.

32. Liu, M.; Tian, H.; Chen, G.; Ren, W.; Zhang, C.; Liu, J. Effects of land-use and land-cover change on evapotranspiration and water yield in China during 1900–2000. *JAWRA J. Am. Water Resour. Assoc.* **2008**, *44*, 1193–1207.

33. Zhou, L.; Zhou, G. Measurement and modelling of evapotranspiration over a reed (phragmites australis) marsh in northeast China. *J. Hydrol.* **2009**, *372*, 41–47.

34. Fisher, J.B.; Tu, K.P.; Baldocchi, D.D. Global estimates of the land–atmosphere water flux based on monthly AVHRR and ISLSCP-II data, validated at 16 FLUXNET sites. *Remote Sens. Environ.* **2008**, *112*, 901–919.

35. Fisher, J.B.; Lee, B.; Purdy, A.J.; Halverson, G.H.; Dohlen, M.B.; Cawse-Nicholson, K.; Wang, A.; Anderson, R.G.; Aragon, B.; Arain, M.A.; et al. ECOSTRESS: NASA's Next Generation Mission to Measure Evapotranspiration from the International Space Station. *Water Resour. Res.* **2020**, *56*, e2019WR026058.

36. Ershadi, A.; McCabe, M.F.; Evans, J.P.; Chaney, N.W.; Wood, E.F. Multi-site evaluation of terrestrial evaporation models using FLUXNET data. *Agric. For. Meteorol.* **2014**, *187*, 46–61.

37. Xie, Z.; Yao, Y.; Li, Y.; Liu, L.; Ning, J.; Yu, R.; Fan, J.; Kan, Y.; Zhang, L.; Xu, J.; et al. Satellite-based PT-SinRH evapotranspiration model: Development and validation from AmeriFlux data. *Remote Sens.* **2024**, *16*, 2783. [CrossRef]

38. Reichstein, M.; Subke, J.A.; Angeli, A.C.; Tenhunen, J.D. Does the temperature sensitivity of decomposition of soil organic matter depend upon water content, soil horizon, or incubation time? *Glob. Change Biol.* **2005**, *11*, 1754–1767.

39. Twine, T.E.; Kustas, W.; Norman, J.; Cook, D.; Houser, P.; Meyers, T.; Prueger, J.; Starks, P.; Wesely, M. Correcting eddy-covariance flux underestimates over a grassland. *Agric. For. Meteorol.* **2000**, *103*, 279–300.

40. Foken, T. The energy balance closure problem: An overview. *Ecol. Appl.* **2008**, *18*, 1351–1367.

41. Xiao, Z.; Liang, S.; Tian, X.; Jia, K.; Yao, Y.; Jiang, B. Reconstruction of Long-Term Temporally Continuous NDVI and Surface Reflectance from AVHRR Data. *IEEE J. Sel. Top. Appl. Earth Obs. Remote Sens.* **2017**, *10*, 5551–5568.

42. Priestley, C.H.B.; Taylor, R.J. On the Assessment of Surface Heat Flux and Evaporation Using Large Scale Parameters. *Mon. Weather. Rev.* **1972**, *100*, 81–92.

43. Jin, Y.; Randerson, J.T.; Goulden, M.L. Continental-scale net radiation and evapotranspiration estimated using MODIS satellite observations. *Remote Sens. Environ.* **2011**, *115*, 2302–2319.

44. Liu, M.; Adam, J.C.; Richey, A.S.; Zhu, Z.; Myneni, R.B. Factors controlling changes in evapotranspiration, runoff, and soil moisture over the conterminous U.S.: Accounting for vegetation dynamics. *J. Hydrol.* **2018**, *565*, 123–137.

45. Ryu, Y.; Baldocchi, D.D.; Ma, S.; Hehn, T. Interannual variability of evapotranspiration and energy exchange over an annual grassland in California. *J. Geophys. Res. Atmos.* **2008**, *113*, D09104.

46. Seneviratne, S.I.; Lehner, I.; Gurtz, J.; Teuling, A.J.; Lang, H.; Moser, U.; Grebner, D.; Menzel, L.; Schroff, K.; Vitvar, T.; et al. Swiss prealpine Rietholzbach research catchment and lysimeter: 32 year time series and 2003 drought event. *Water Resour. Res.* **2012**, *48*, W06526.

47. Liu, Y.; Parolari, A.J.; Kumar, M.; Huang, C.W.; Katul, G.G.; Porporato, A. Increasing atmospheric humidity and CO_2 concentration alleviate forest mortality risk. *Proc. Natl. Acad. Sci. USA* **2017**, *114*, 9918–9923.

48. Tian, Y.; Zou, C.Z.; Mitchell, K.E.; Wong, V.; Kogan, F.N.; Jiang, L.; Zhan, X. Improvements of numerical weather predictions using a new AVHRR green vegetation fraction dataset, in Atmospheric and Environmental Remote Sensing Data Processing and Utilization IV: Readiness for GEOSS II. *Int. Soc. Opt. Photonics* **2008**, *7085*, 70850N.

49. Henn, B.; Painter, T.H.; Bormann, K.J.; McGurk, B.; Flint, A.L.; Flint, L.E.; White, V.; Lundquist, J.D. High-Elevation Evapotranspiration Estimates During Drought: Using Streamflow and NASA Airborne Snow Observatory SWE Observations to Close the Upper Tuolumne River Basin Water Balance. *Water Resour. Res.* **2018**, *54*, 746–766.

50. Long, D.; Pan, Y.; Zhou, J.; Chen, Y.; Hou, X.; Hong, Y.; Scanlon, B.R.; Longuevergne, L. Global analysis of spatiotemporal variability in merged total water storage changes using multiple GRACE products and global hydrological models. *Remote Sens. Environ.* **2017**, *192*, 198–216.

51. Martens, B.; Waegeman, W.; Dorigo, W.A.; Verhoest, N.E.C.; Miralles, D.G. Terrestrial evaporation response to modes of climate variability. *npj Clim. Atmos. Sci.* **2018**, *1*, 43.

52. Miralles, D.G.; Teuling, A.J.; van Heerwaarden, C.C.; de Arellano, J.V.G. Mega-heatwave temperatures due to combined soil desiccation and atmospheric heat accumulation. *Nat. Geosci.* **2014**, *7*, 345–349.

53. Lesinger, K.; Tian, D. Trends, Variability, and Drivers of Flash Droughts in the Contiguous United States. *Water Resour. Res.* **2022**, *58*, e2022WR032186.

54. Guo, X.; Yao, Y.; Tang, Q.; Liang, S.; Shao, C.; Fisher, J.B.; Chen, J.; Jia, K.; Zhang, X.; Shang, K. Multimodel ensemble estimation of Landsat-like global terrestrial latent heat flux using a generalized deep CNN-LSTM integration algorithm. *Agric. For. Meteorol.* **2024**, *349*, 109962.

55. Vecchi, G.A.; Wittenberg, A.T. El Niño and our future climate: Where do we stand? *WIREs Clim. Chang.* **2010**, *1*, 260–270.

56. Nemani, R.R.; Keeling, C.D.; Hashimoto, H.; Jolly, W.M.; Piper, S.C.; Tucker, C.J.; Myneni, R.B.; Running, S.W. Climate-Driven Increases in Global Terrestrial Net Primary Production from 1982 to 1999. *Science* **2003**, *300*, 1560–1563. [PubMed]

57. Yang, Y.; Roderick, M.L.; Guo, H.; Miralles, D.G.; Zhang, L.; Fatichi, S.; Luo, X.; Zhang, Y.; McVicar, T.R.; Tu, Z.; et al. Evapotranspiration on a greening Earth. *Nat. Rev. Earth Environ.* **2023**, *4*, 626–641.

58. Xiao, J.; Sun, G.; Chen, J.; Chen, H.; Chen, S.; Dong, G.; Gao, S.; Guo, H.; Guo, J.; Han, S.; et al. Carbon fluxes, evapotranspiration, and water use efficiency of terrestrial ecosystems in China. *Agric. For. Meteorol.* **2013**, *182–183*, 76–90.

59. Hu, Z.; Wu, G.; Zhang, L.; Li, S.; Zhu, X.; Zheng, H.; Zhang, L.; Sun, X.; Yu, G. Modeling and Partitioning of Regional Evapotranspiration Using a Satellite-Driven Water-Carbon Coupling Model. *Remote Sens.* **2017**, *9*, 54. [CrossRef]